Sensors and Materials, Vol. 38, No. 8 (2026) 4937–4962
MYU Tokyo

S & M 4603

Tidal Effect on Potential Storm Surge Hazards at a Nuclear Power Plant Site on Korea's West Coast

Taegeon Hwang,[1] Hyeon-Jeong Kim,[2] Byung-Il Min,[2]
Minjang Seo,[3] and Woo-Dong Lee[4*]

[1]Institute of Marine Industry, Gyeongsang National University,
2, Tongyeonghaean-ro, Tongyeong-si, Gyeongsangnam-do 53064, Republic of Korea
[2]Environmental Safety Technology Research Division, Korea Atomic Energy Research Institute,
111, Daedeok-daero 989 beon-gil, Yuseong-gu, Daejeon 34057, Republic of Korea
[3]Harbor & Coastal Department, Yooshin Engineering Corporation,
24, Boramae-ro 5 ga-gil, Dongjak-gu, Seoul 07071, Republic of Korea
[4]Department of Ocean Civil Engineering, Gyeongsang National University,
2, Tongyeonghaean-ro, Tongyeong-si, Gyeongsangnam-do 53064, Republic of Korea

(Received December 1, 2025; accepted August 12, 2026)

Keywords: tide–surge interaction, coastal hazard assessment, typhoon parameters, sensitivity analysis, macrotidal coast, coastal nuclear power plant safety

In this study, we examine how tides affect potential storm surge hazards at the Hanbit Nuclear Power Plant on Korea's west coast, a macrotidal region characterized by large tidal ranges. Using 33 synthetic typhoon scenarios generated using the Tropical Cyclone Risk Model, we performed tide–storm surge interaction (TSSI) simulations with the ADvanced CIRCulation model to assess nonlinear effects between tides and storm surges. Model performance was validated against water-level observations during Typhoons Muifa (1109) and Bolaven (1215), demonstrating high accuracy in reproducing tidal phases and maximum water levels. The results show that tidal interaction significantly increases total water levels while reducing the intrinsic storm surge component through nonlinear TSSI associated with the tidal phase, modified sea-surface slope, velocity-field changes, and bottom-friction effects. On average, the maximum storm surge height (MSSH) and time-integrated storm surge height (TISSH) from TSSI simulations were 70.94 and 77.19% of those from storm-surge-only (SSO) simulations, respectively. In contrast, the average maximum water surface height (MWSH) corresponded to 94.76% of the linear sum of SSO-based MSSH and the peak tidal level, indicating that simple linear superposition may overestimate extreme water levels. A sensitivity analysis showed that central pressure and maximum wind speed were the dominant factors for MSSH and TISSH, respectively, whereas the closest approach distance was consistently the least influential. Validation using water-level sensor records from tide-gauge stations supports the reliability of the numerical simulations, and the findings highlight the necessity of a TSSI-based hazard assessment for coastal nuclear facilities in macrotidal environments.

*Corresponding author: e-mail: wdlee@gnu.ac.kr
https://doi.org/10.18494/SAM6204

ISSN 0914-4935 © MYU K.K.
https://myukk.org/

1. Introduction

The west coast of the Korean Peninsula is globally recognized as a macrotidal environment. Yeonggwang, where the Hanbit Nuclear Power Plant (HNPP) is located, exhibits an extreme tidal range of approximately 769.6 cm, which strongly affects storm-driven water-level dynamics during typhoon events. Unusually high sea levels can occur when typhoon-induced storm surges coincide with high tide. In other macrotidal regions, such as Hangzhou Bay in China and Delaware Bay in the United States, tide–storm surge interaction (TSSI) has been reported to amplify total water levels by more than 50%.(1) Therefore, in environments with extreme tidal ranges, the potential impacts of storm surges under tidal conditions must be considered when assessing coastal hazard risks associated with typhoons. This consideration is fundamental for ensuring the safe and reliable operation of high-risk coastal infrastructure, including nuclear power plants. Simulations of Hurricane Rita (AL182005) using the Finite Volume Community Ocean Model (FVCOM) demonstrated that the maximum water level caused by storm surge can be amplified by up to approximately 70% of the tidal range through the combined effects of tides and bathymetry.(2) A study of the November 2007 North Sea storm and the March 2008 Atlantic storm in the English Channel showed that TSSI can increase storm-induced water levels by up to 0.74 m.(3) The same study also revealed that maximum water levels can rise by roughly 50% at several locations, and it was pointed out that treating tides and storm surges independently can lead to the systematic underestimation of flood hazards. A numerical study of the southern sector of the West Sea demonstrated that tidal phase plays a significant role in surge prediction.(4) The study showed that TSSI is relatively weak over gently sloping shelves, while in coastal regions with abrupt depth transitions, tidal phase has a strong effect on storm-surge-induced water levels. When storm surges occur near high tide, an additional amplification of approximately 0.4 m can develop. These findings indicate that tidal phase is a key factor governing the spatial and temporal distributions of storm surge heights. In a similar study, FVCOM-based simulations for Delaware Bay showed that TSSI generally amplifies storm-induced water levels.(5) Analysis of tide-gauge observations from 65 stations across the North Atlantic further confirmed that TSSI produces pronounced amplitude oscillations.(6) A global-scale assessment also demonstrated that concurrent tides and storm surges during spring tide can increase maximum water levels by approximately 0.5 to 1.5 m.(7) They also noted that in regions such as northwestern Australia and La Rochelle in France, the temporal alignment between tidal phase and peak surge height plays a major role in generating extreme sea levels. An investigation of Cyclone Aila (0902) in the upper Bay of Bengal revealed a strongly asymmetric TSSI response.(8) When storm surges coincided with the rising limb of the tide, water levels increased by about 0.5 to 0.9 m. In contrast, during the falling limb, peak surge heights decreased by approximately 15%. These findings highlight tidal phase as a major source of uncertainty in storm surge prediction and emphasize the necessity of explicitly resolving TSSI in coupled hydrodynamic models.

Sea-level rise (SLR) associated with climate change has recently been identified as an additional factor that intensifies TSSI. A comparative analysis of storm surge characteristics for the periods 1979–2014 and 2040–2100 under SLR scenarios showed notable changes in surge behavior.(9) Specifically, the 10-year return level of extreme total water levels was projected to increase by an average of 0.34 m and by up to 0.5 m in some regions. A similar tendency was observed in the Pearl River Delta, where deeper water induced by SLR was found to amplify tidal ranges by up to 0.5 m and consequently increase maximum total water levels.(10) These studies suggest that interactions among tide, storm surge, and SLR collectively increase local sea levels and amplify coastal hazard risk.

On the other hand, several studies have shown that while tides increase the total water level, they may reduce the intrinsic storm surge response depending on tidal phase. Numerical simulations of Typhoon Chan-hom (1509) along the southeastern coast of China showed that TSSI tends to suppress storm surge heights near high tide while enhancing them near low tide.(11) A comparative analysis of Typhoons Mangkhut (1826) and Barijat (1827) in the northern South China Sea showed that both the sign and magnitude of TSSI vary depending on storm track and tidal range.(12) It was also shown that nonlinear effects in shallow coastal waters can reduce maximum storm surge heights (MSSHs) by up to 30%. This result demonstrates that tidal phase can both amplify and reduce peak storm surges depending on environmental conditions.

Overall, previous studies indicate that TSSI is not a linear superposition but rather a nonlinear process influenced by tidal phase, typhoon track, bathymetry, and water depth. For critical coastal assets such as nuclear power plants, hazard assessments must incorporate typhoon-related meteorological forcing, tidal interaction, and site-specific geomorphology. In a previous investigation, storm surge heights along the West Sea coast were examined using combinations of historical typhoons that had affected the Korean Peninsula.(13) In another study, 33 synthetic typhoons generated by the Tropical Cyclone Risk Model (TCRM) were selected to quantify the potential storm surge hazard at the HNPP site.(14) However, despite the macrotidal nature of Korea's West Sea, storm-surge-only (SSO) simulations that did not account for tidal effects were employed in both studies.

Therefore, in the present study, we aim to quantify the effect of tides on storm surge near HNPP during typhoon passage. Coupled TSSI simulations are performed using the ADvanced CIRCulation (ADCIRC) model, and a conservative scenario in which a typhoon passes near HNPP at high tide is considered. In this scenario, the timing of typhoon forcing is adjusted relative to the astronomical tide to examine the storm surge response under high-water conditions. Using the results of these simulations, we analyze the effects of typhoon meteorological parameters (central pressure, maximum wind speed, and radius of maximum wind speed) and the closest approach distance on water-level rise. With model reliability supported by validation against water-level sensor records from tide-gauge stations, the potential storm surge hazard at the HNPP site is subsequently evaluated with explicit consideration of TSSI.

2. Methodology

2.1 Numerical model

2.1.1 Governing equations

ADCIRC is a depth-integrated hydrodynamic model that uses an unstructured triangular finite-element mesh and is suitable for simulating long-period water-level variations such as tides, storm surges, and tsunamis over large coastal domains.(15) In this study, the two-dimensional depth-integrated (2DDI) formulation was employed. The governing equations are expressed as follows:

$$\frac{\partial \zeta}{\partial t}+\frac{1}{R\cos\Phi}\frac{\partial UH}{\partial \Lambda}+\frac{1}{R}\frac{\partial VH}{\partial \Phi}-\frac{VH\tan\Phi}{R}=0, \tag{1}$$

$$\begin{aligned}&\frac{\partial U}{\partial t}+\frac{U}{R\cos\Phi}\frac{\partial U}{\partial \Lambda}+\frac{V}{R}\frac{\partial U}{\partial \Phi}-\left(\frac{U\tan\Phi}{R}+f\right)V\\&=-\frac{1}{R\cos\Phi}\frac{\partial}{\partial \Lambda}\left[\frac{P_s}{\rho_0}+g\left(\zeta-\alpha\eta\right)\right]+\frac{\tau_{s\Lambda}}{\rho_0 H}-\frac{\tau_{b\Lambda}}{\rho_0 H}+M_\Lambda+D_\Lambda-B_\Lambda,\end{aligned} \tag{2}$$

$$\begin{aligned}&\frac{\partial V}{\partial t}+\frac{U}{R\cos\Phi}\frac{\partial V}{\partial \Lambda}+\frac{V}{R}\frac{\partial V}{\partial \Phi}+\left(\frac{U\tan\Phi}{R}+f\right)U\\&=-\frac{1}{R}\frac{\partial}{\partial \Phi}\left[\frac{P_s}{\rho_0}+g\left(\zeta-\alpha\eta\right)\right]+\frac{\tau_{s\Phi}}{\rho_0 H}-\frac{\tau_{b\Phi}}{\rho_0 H}+M_\Phi+D_\Phi-B_\Phi,\end{aligned} \tag{3}$$

where t is time, ζ is the free-surface elevation relative to mean sea level, R is Earth's radius, Λ and Φ denote longitude and latitude, respectively, f is the Coriolis parameter, g is gravitational acceleration, α is the Earth's elasticity factor, η is the equilibrium tidal potential, ρ_0 is water density, P_s is atmospheric pressure at the sea surface, H is the total water depth defined as the geoid depth h plus ζ, U and V are depth-averaged velocity components, UH and VH represent volume transports per unit width, $\tau_{s\Lambda}$ and $\tau_{s\Phi}$ denote wind stresses, $\tau_{b\Lambda}$ and $\tau_{b\Phi}$ denote bottom stresses, M_Λ and M_Φ are gradients of depth-averaged lateral stresses, D_Λ and D_Φ are turbulent diffusion terms, and B_Λ and B_Φ are baroclinic pressure-gradient terms. In the present simulations, these forcing, stress, diffusion, and pressure-gradient terms were treated following the standard ADCIRC numerical implementation.(15)

2.1.2 Tidal and meteorological forcing

At the open boundary, astronomical tides were generated using the eight principal tidal constituents (M_2, S_2, N_2, K_2, K_1, O_1, P_1, Q_1). Water levels were calculated using the following harmonic representation:

$$\eta(\Lambda,\Phi,t) = \sum C_{jn} f_{jn}(t_0) L_j(\Phi) \cos\left[\frac{2\pi(t-t_0)}{T_{jn}} + j\Lambda + v_{jn}(t_0)\right], \tag{4}$$

where C_{jn} is the amplitude of tidal constituent $n, f_{jn}(t_0)$ is the nodal correction factor, j (= 0, 1, 2) denotes the spherical harmonic degree with $L_0 = 3\sin^2(\Phi) - 1$, $L_1 = \sin(2\Phi)$, and $L_2 = \cos^2(\Phi)$, t_0 is the reference time, T_{jn} is the tidal period, and $v_{jn}(t_0)$ is the astronomical argument.

The harmonic constants were derived from established formulations(16,17) and computed using a harmonic analysis package.(18) The external meteorological forcing applied to ADCIRC consists of the pressure field $P(r, \theta)$ and the wind field $V(r)$. Both fields were generated using the parametric formulation(19) with typhoon parameters obtained from TCRM. The pressure and wind fields are given by

$$P(r,\theta) = P_c + (P_s - P_c)\exp^{-\left[R_{max}(\theta)/r\right]^B}, \tag{5}$$

$$V(r) = \sqrt{\frac{B}{\rho_a}\left(\frac{R_{max}(\theta)}{r}\right)^B (P_s - P_c)\exp^{-\left[R_{max}(\theta)/r\right]^B} + \left(\frac{rf}{2}\right)^2} - \frac{rf}{2}, \tag{6}$$

where r is the radial distance from the typhoon center, θ denotes the azimuth, P_c is the central pressure, ρ_a denotes air density, and B is the Holland shape parameter, which typically ranges from 1 to 2.5.

An additional parameter required to define the typhoon structure is the radius of maximum wind speed (R_{max}). In this study, R_{max} was estimated using the empirical relationship(20)

$$R_{max} = 0.0011 \times \exp\left[0.0109 P_c(t)\right], \tag{7}$$

where $P_c(t)$ is the time-dependent central pressure.

2.2 Typhoon scenarios

2.2.1 Probabilistic approach

TCRM is a statistical wind-field synthesis model developed to assess extreme wind and storm surge hazards associated with tropical cyclones. The model generates synthetic typhoon scenarios by analyzing the historical observations of typhoons. To address the limitation that the observational record of tropical cyclones is relatively short and that time-series information is therefore constrained, TCRM employs a first-order autoregressive (AR-1) process.

TCRM consists of five major components: a data-processing module, a track-generation module, a wind-field module, a statistical module, and a hazard-assessment module. The model analyzes the temporal and spatial occurrences of historical typhoons, including their genesis location, track, central pressure, and maximum wind speed, and synthesizes typhoons by preserving their statistical characteristics and correlation structure. The synthetic typhoon generation procedure and its underlying statistical algorithms are described in detail elsewhere.(21)

In TCRM, the translational speed $v(t)$ and the central pressure tendency $P_c(t)$ of a typhoon are expressed as

$$v(t) = \mu_v^i + \sigma_v^i \chi_v^i(t), \tag{8}$$

$$\chi_v^i(t) = \alpha_v^i \chi_v^i(t-1) + \Phi_v^i \varepsilon, \tag{9}$$

$$P_c(t) = P_c(t-1) + \dot{p}(t)\Delta t, \tag{10}$$

$$\dot{p}(t) = \mu_p^i + \sigma_p^i \chi_p^i(t), \tag{11}$$

$$\chi_p^i(t) = \alpha_p^i \chi_p^i(t-1) + \Phi_p^i \varepsilon, \tag{12}$$

where μ_v^i and μ_p^i represent the mean translational speed and mean central pressure at grid cell i, σ_v^i and σ_p^i denote the corresponding standard deviations, α_v^i and α_p^i are the AR-1 autocorrelation coefficients, ε is a logistic random variable with mean 0 and variance 0.286, and Φ_v^i and Φ_p^i denote the variance-scaling parameters for translational speed and central pressure, respectively.

2.2.2 Selection of synthetic typhoons

For this study, the International Best Track Archive for Climate Stewardship (IBTrACS) database was used.(22) The analysis included all typhoons that occurred in the northwestern Pacific from 1848 to 2020. The spatial domain for synthetic typhoon generation was defined as 0–55°N and 100–170°E.

A total of approximately 3000 synthetic typhoons with a 100-year return period were generated within this spatial domain. Among these synthetic typhoons, the tracks that approached north of 30°N and passed within 120–135°E were first screened because they were considered capable of affecting the west coast of the Korean Peninsula, including the HNPP site. Through this spatial screening, 33 synthetic typhoons were selected for the storm surge simulations. The ranges of minimum P_c, along with the corresponding $V_{\max}$ and $R_{\max}$, and $D_{\min}$ for each selected typhoon are as follows.

- Minimum central pressure (P_c): 915–985 hPa
- Maximum wind speed ($V_{\max}$): 26.52–68.34 m/s
- Radius of maximum wind speed ($R_{\max}$): 24.08–50.00 km
- Closest approach distance ($D_{\min}$) to HNPP: 0.458–532.72 km

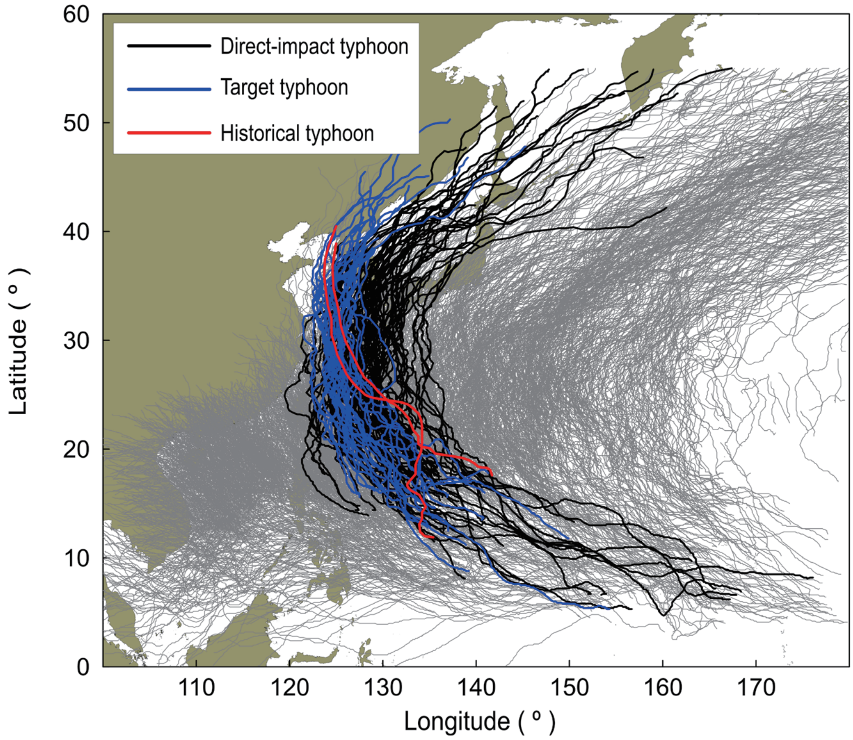

Fig. 1. (Color online) Tracks of synthetic and historical typhoons used for TSSI simulations.

The selected synthetic typhoons are shown together with historical typhoons in Fig. 1. The selected synthetic typhoons were used to investigate TSSI at the HNPP site.

2.3 Computational domain and grid configuration

The computational mesh used in this study consists of an unstructured triangular grid based on spherical coordinates, and node locations are defined using latitude and longitude referenced to WGS84. The computational domain covers the Korean Peninsula, most of Japan except Hokkaido, Taiwan, and the surrounding region of the Ogasawara Islands, representing a portion of the northwestern Pacific.

Coarse grid resolution was assigned to offshore regions, whereas fine-resolution elements with a spacing of approximately 10 m were applied near the HNPP coastline to improve simulation accuracy. The final grid consists of 398909 elements and 216241 nodes.

Tides were generated along the offshore boundary, which is shown by the blue outline in Fig. 2. The tidal simulation was first run for approximately three days to allow tidal motion to reach dynamic equilibrium around the Korean Peninsula. After tidal stabilization, the typhoon fields were applied to conduct the TSSI simulations. To construct the conservative high-tide scenario at the HNPP site, the timing of the meteorological forcing fields was shifted with respect to the astronomical tide so that the MSSH occurred at the high-water phase. The typhoon track and

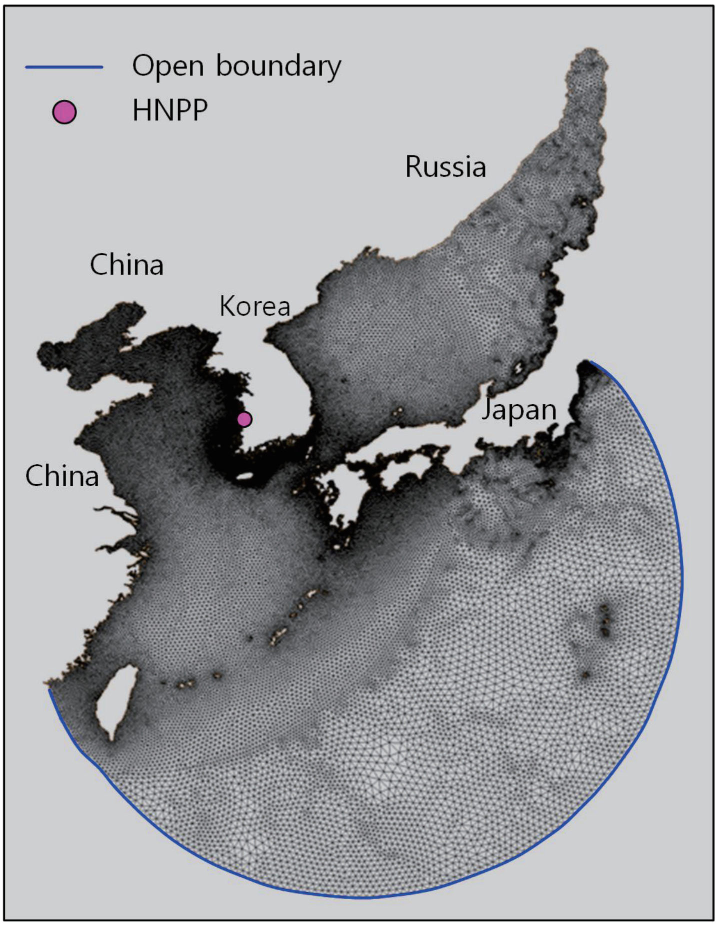

Fig. 2. (Color online) Grid configuration used for TSSI simulations.

intensity parameters were not modified; only the reference time of the wind and pressure fields was adjusted.

2.4 Model validation

To evaluate the validity and reproducibility of ADCIRC in simulating TSSI, model-computed water levels were compared with tide-gauge observations recorded during the passages of Typhoons Muifa (1109) and Bolaven (1215). The locations of the tide-gauge stations used for validation are shown in Fig. 3. A total of 19 stations were considered, including eight along the West Sea coast, five along the south coast, three along the east coast, two around Jeju Island, and one at Ulleungdo.

Before the typhoons affected the Korean Peninsula, observed tidal elevations at the Yeonggwang and Mokpo tide-gauge stations were compared with the corresponding ADCIRC simulations. These results are presented in Fig. 4, and Fig. 5 shows the observed and simulated water-surface heights during the periods affected by the two typhoons. In addition, Fig. 6

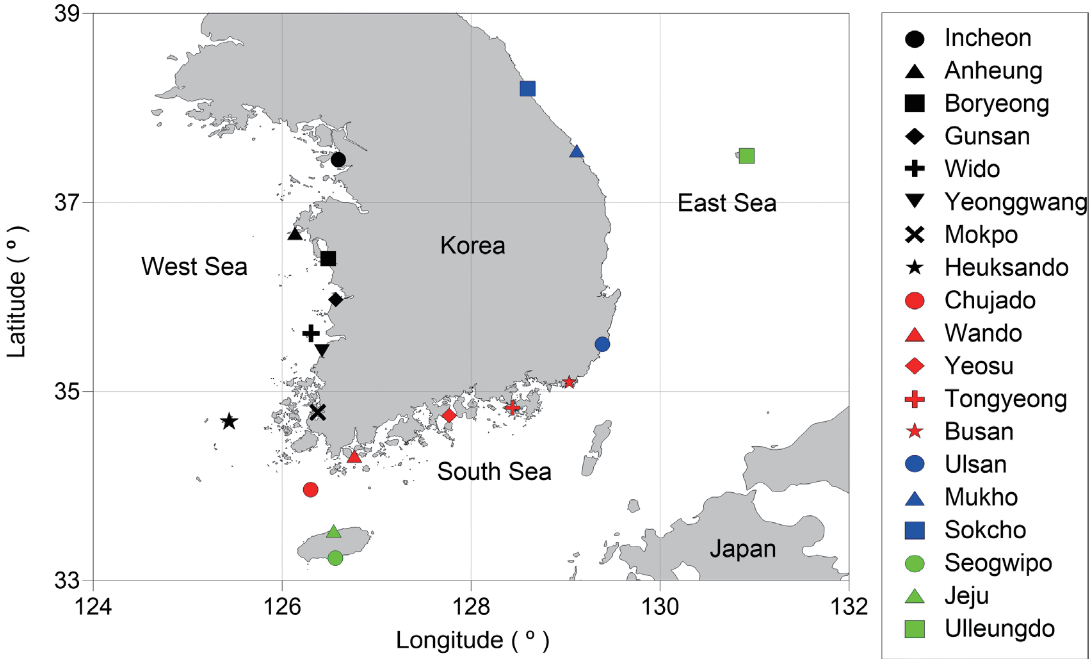

Fig. 3. (Color online) Locations of tide-gauge stations around the Korean Peninsula used for model validation.

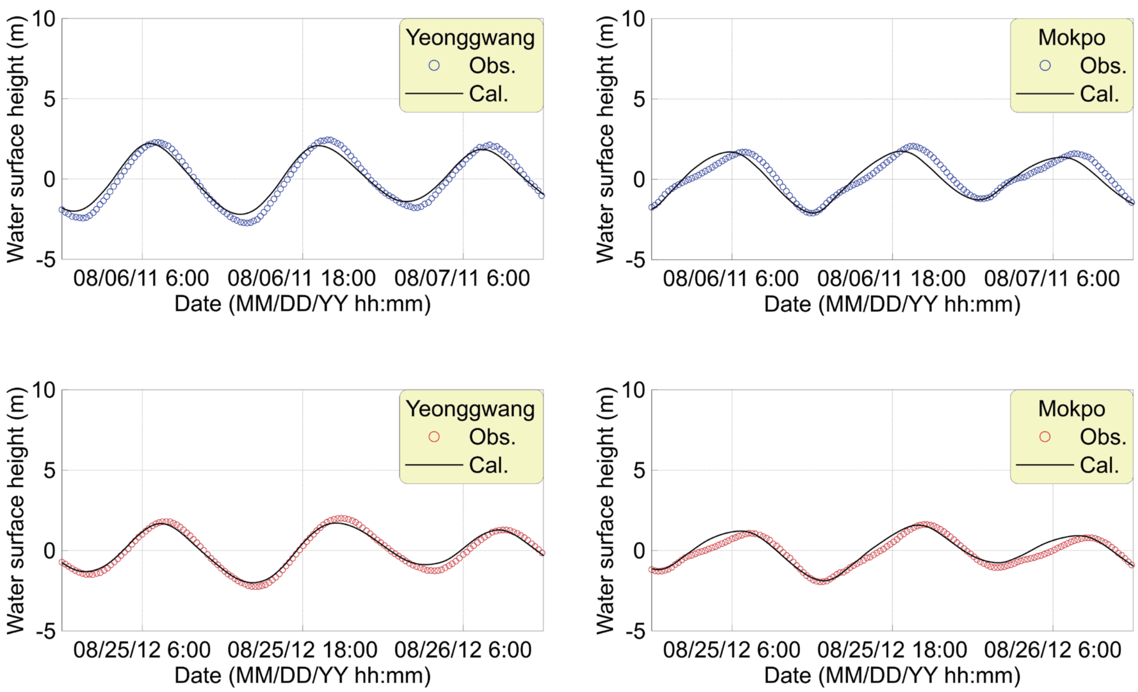

Fig. 4. (Color online) Time series of observed and simulated tidal elevations during periods without typhoon influence for Muifa (upper) and Bolaven (lower).

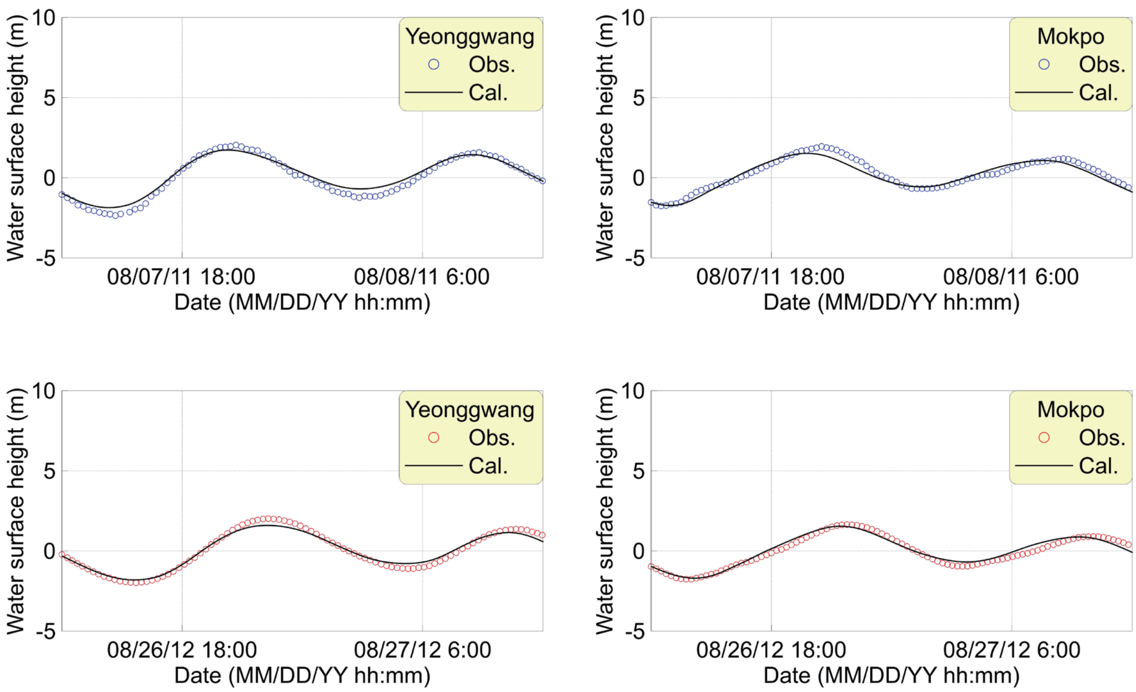

Fig. 5. (Color online) Time series of observed and simulated water-surface heights during Typhoons Muifa (upper) and Bolaven (lower).

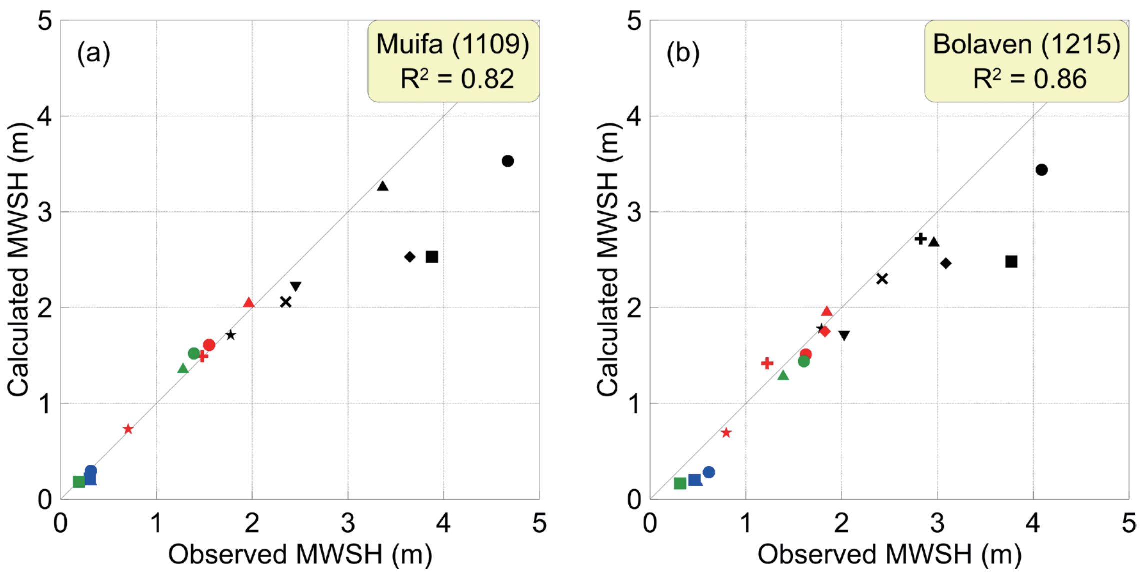

Fig. 6. (Color online) Scatter plots of observed and simulated MWSH values during Typhoons (a) Muifa and (b) Bolaven.

presents scatter plots of the maximum water surface height (MWSH) observed and simulated during each typhoon. During Typhoon Muifa, data gaps occurred at the Wido and Yeosu tide-gauge stations.

As shown in Fig. 4, ADCIRC successfully reproduces tidal variations at the two stations near HNPP under non-typhoon conditions. The coefficient of determination (R^2) supports the statistical reliability of the model performance. Before Typhoon Muifa, the R^2 values at Yeonggwang and Mokpo were 0.92 and 0.86, respectively. Before Typhoon Bolaven, the values were 0.96 and 0.89, respectively, demonstrating similarly strong reproducibility.

As illustrated in Fig. 5, the model also reproduced water-surface variations with high fidelity during the typhoon periods. During Typhoon Muifa, the R^2 values for Yeonggwang and Mokpo were 0.95 and 0.94, respectively. During Typhoon Bolaven, the values were 0.96 and 0.95, respectively, demonstrating consistently strong model performance.

Regarding MWSH estimation, which is essential for coastal hazard assessment, the R^2 values were 0.82 for Muifa and 0.86 for Bolaven. These values indicate statistically meaningful correlations and represent a clear improvement compared with the SSO simulations(14) in which the R^2 values of 0.742 and 0.755 were obtained. This improvement shows that including tidal effects enhances the reproducibility of ADCIRC simulations for storm surge hazard assessment. Overall, these validation results confirm the reliability of ADCIRC when tidal processes are included, thereby supporting its suitability for the TSSI simulations conducted in this study.

3. TSSI Simulation Results

3.1 Spatial distribution of MWSH

Figure 7 presents the spatial distributions of MWSH obtained from the TSSI simulations for synthetic typhoons Nos. 2 and 28. Although the D_{min} values of the two typhoons are comparable at 120.17 and 148.11 km, respectively, their meteorological characteristics differ considerably. Typhoon No. 2 exhibits weaker intensity, higher P_c, lower V_{max}, and larger R_{max}. In contrast, typhoon No. 28 has lower P_c, higher V_{max}, and smaller R_{max}, representing a structurally stronger typhoon.

These differences result in clearly distinguishable spatial patterns of water-level response. Because of its stronger intensity (lower P_c and higher V_{max}) and smaller R_{max}, typhoon No. 28 produces higher MWSH values over a broader area along the western coast of the Korean Peninsula. On the other hand, typhoon No. 2, characterized by weaker intensity and larger R_{max}, passes more than 120 km away from the HNPP site during its northward movement, thereby exerting a relatively limited influence on water-level rise along the West Sea coast.

This trend is consistent with previously reported SSO simulation results.(14) However, because we incorporate tidal processes in the present study, the contribution of storm surge is partially moderated. The nonlinear interaction between tide and surge leads to a spatial storm surge response that is somewhat reduced compared with that of the SSO simulations.

3.2 Water-level response under TSSI conditions

Figure 8 presents the time-domain water-level variations at the HNPP site for synthetic typhoons Nos. 8, 10, and 19. These results clearly illustrate how tidal processes interact with

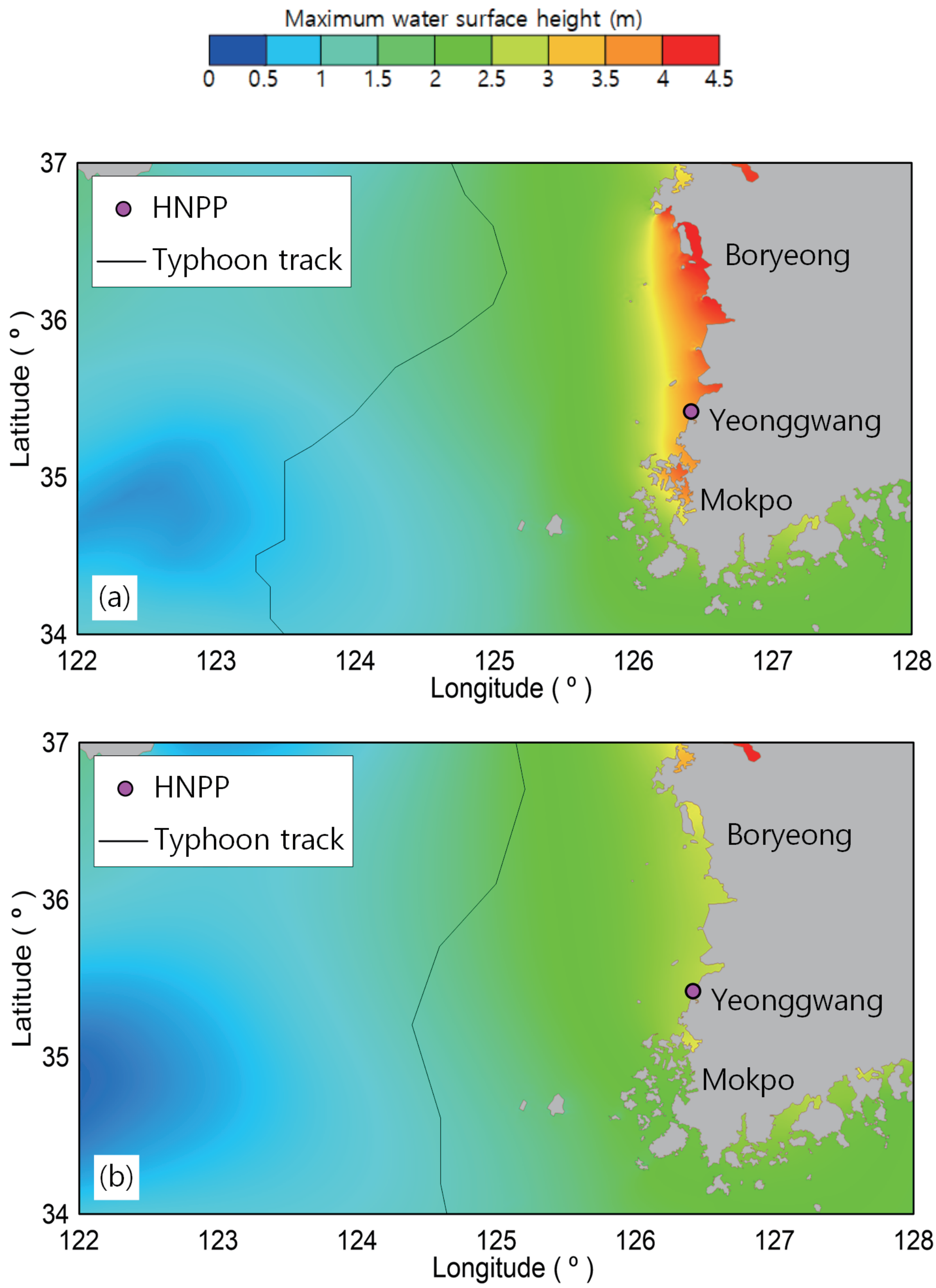

Fig. 7. (Color online) Spatial distributions of MWSH for synthetic typhoons (a) No. 2 and (b) No. 28.

storm surges under TSSI conditions. For comparison, the tidal variability included in the TSSI simulations is also shown. For analytical consistency, the time of peak MWSH for each typhoon is defined as the reference time t_p, and all time series are aligned accordingly.

Typhoon No. 19 generates the highest MWSH because it approaches extremely close to the HNPP site (D_{min} = 4.52 km) and exhibits strong meteorological characteristics (P_c = 951.15 hPa,

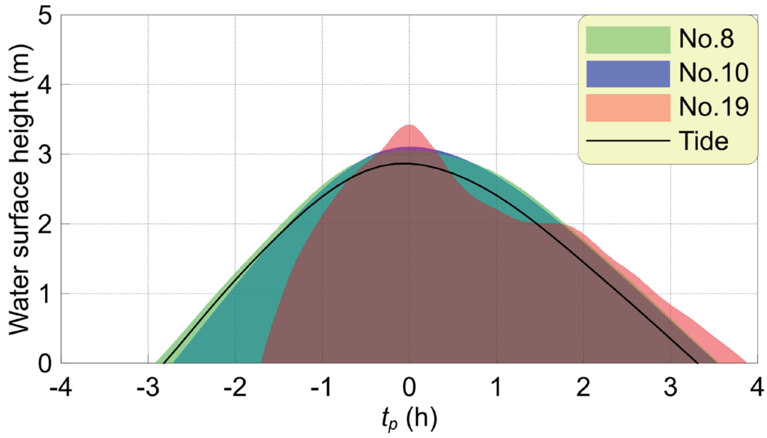

Fig. 8. (Color online) Time series of water-surface heights and tide levels at the HNPP site for synthetic typhoons Nos. 8, 10, and 19.

V_{max} = 47.13 m/s, and R_{max} = 35.61 km). These conditions produce a rapid rise in water level over a short period.

In contrast, typhoons Nos. 8 and 10 exhibit meteorological similarities, with P_c values of 983 and 982.04 hPa and V_{max} values of 28.29 and 28.79 m/s, respectively. However, their D_{min} values differ significantly: 188.2 km for No. 8 and 84.39 km for No. 10. As a result, both typhoons produce smaller MWSH values than typhoon No. 19. Their water-level responses show broader and more gradual temporal distributions dominated by tidal fluctuations. For typhoon No. 10, the smaller D_{min} leads to a slightly higher MWSH than typhoon No. 8, yet the rise phase remains relatively narrow. This behavior is consistent with a previous finding that the numerous islands located to the south–southwest of HNPP function as natural breakwaters, mitigating storm surge amplification along this sector of the coast.(14)

Owing to the macrotidal nature of the West Sea, tidal periods are considerably longer than the effective forcing duration of storm surges. As a result, clear storm surge signatures such as those typically distinguishable under SSO conditions are less apparent in TSSI simulations.

Results of previous studies have emphasized that not only the peak water level but also the temporal volume (or area) of the water-level curve is a critical indicator for storm surge hazard assessment.(14,23) Following the approach established in previous studies,(24,25) the time-integrated water surface height (TIWSH) was computed as

$$TIWSH = \int_{t_1}^{t_2} \zeta(t)dt\,. \tag{13}$$

TIWSH simultaneously incorporates both the duration and magnitude of storm-surge-induced water-level variations, providing a more quantitative indicator for assessing potential overtopping and inundation risks.

3.3 Effects of meteorological factors and closest approach distance

Figures 9 and 10 present scatter plots of MWSH and TIWSH, respectively, computed at the HNPP site for the 33 synthetic typhoons. Panels (a)–(d) in each figure show the relationships of MWSH (or TIWSH) with P_c, V_{max}, R_{max}, and D_{min}, respectively.

The MWSH scatter patterns in Fig. 9 show a clear tendency consistent with the SSO results: typhoons with lower P_c and higher V_{max} produce higher MWSH. This occurs because low atmospheric pressure drives SLR while wind-driven stress directly amplifies the storm surge. In addition, since stronger typhoons generally exhibit smaller R_{max},[26] the increasing MWSH with decreasing R_{max} shown in Fig. 9(c) reflects this inverse relationship. Figure 9(d) also shows a general increase in MWSH as the typhoon approaches the HNPP site (smaller D_{min}), although the island-shielding effect described above weakens this trend.

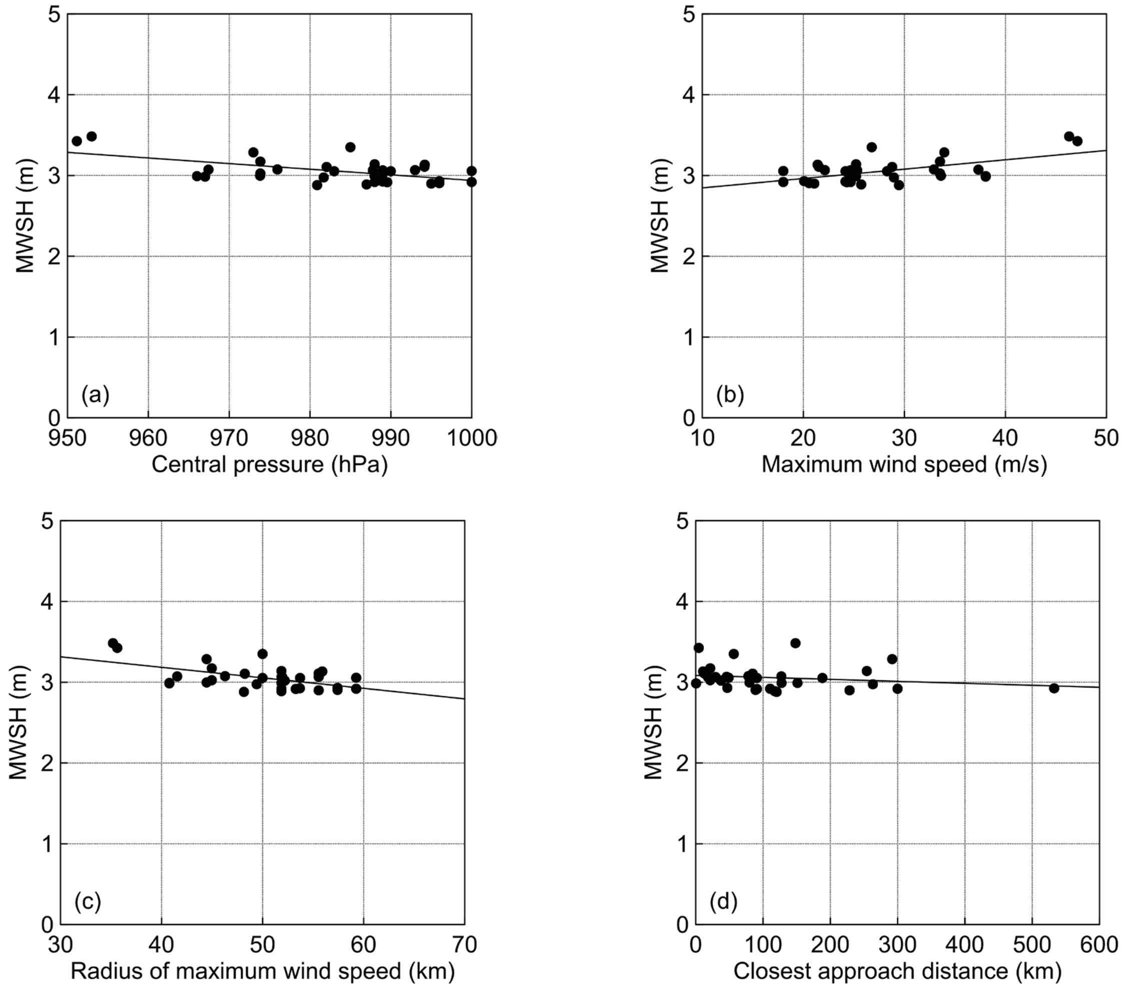

Fig. 9. Scatter plots showing MWSH at the HNPP site as functions of (a) P_c, (b) V_{max}, (c) R_{max}, and (d) D_{min}.

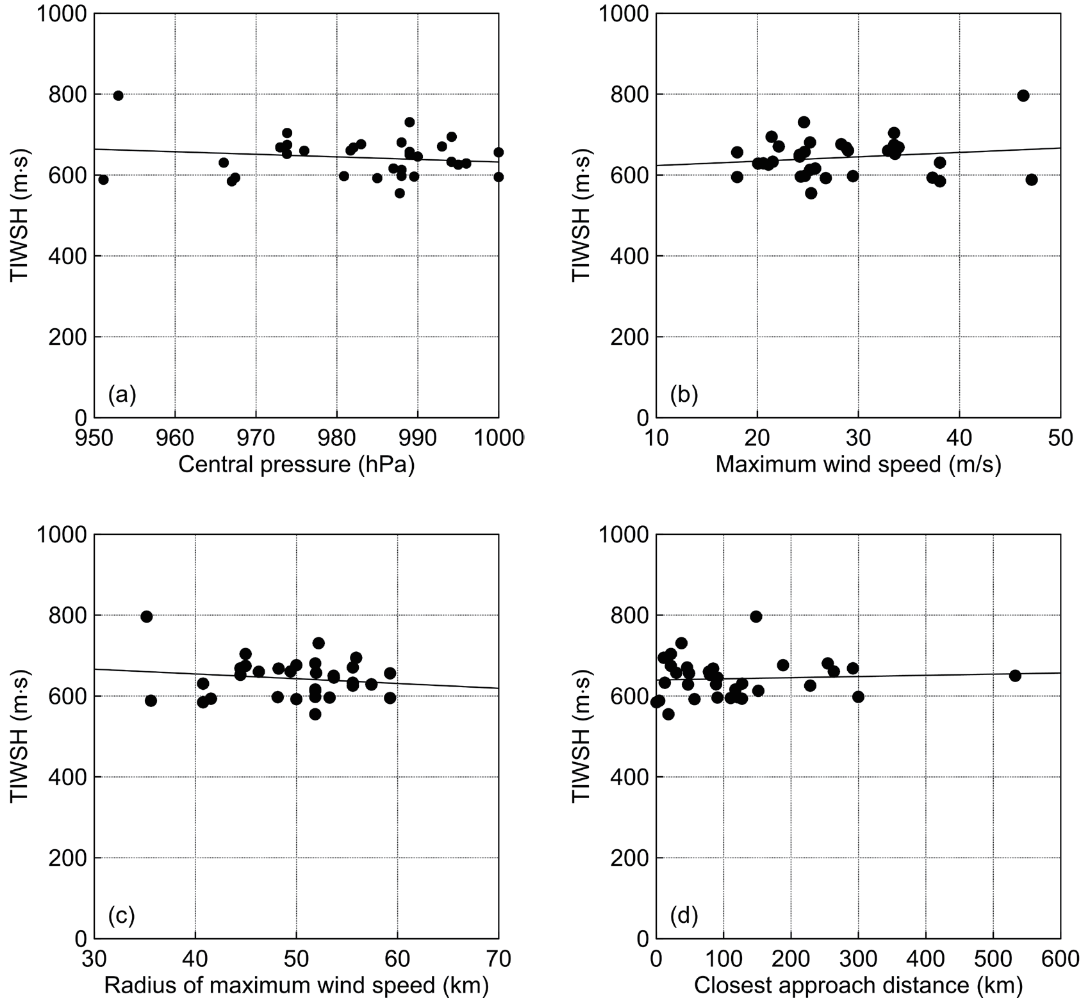

Fig. 10. Scatter plots showing TIWSH at the HNPP site as functions of (a) P_c, (b) $V_{\max}$, (c) $R_{\max}$, and (d) $D_{\min}$.

The TIWSH results in Fig. 10 exhibit overall characteristics similar to those of MWSH. Larger and stronger typhoons produce greater TIWSH because both the duration and magnitude of the water-level response increase. However, TIWSH is more sensitive than MWSH to the combined effects of meteorological parameters and closest approach distance, resulting in a broader spread of data points. This is because TIWSH reflects not only the peak water level but also the temporal evolution and integrated volume of the entire water-level curve.

In contrast, the SSO analysis showed a nonlinear pattern in which TIWSH initially increased and then decreased as $D_{\min}$ increased.[14] The increase was attributed to a longer surge propagation time for more distant typhoons, followed by a decrease once the surge amplitude became too small. Under TSSI conditions, however, this nonlinear response is not evident because tidal processes dominate over the surge signal in the macrotidal environment of the West Sea.

Overall, both MWSH and TIWSH increase with higher typhoon intensity, but the effect of meteorological parameters is moderated under TSSI conditions owing to the dominant effect of tides. This indicates that, in macrotidal regions such as the West Sea, the tidal phase at the time of landfall is as important as typhoon intensity and track characteristics when assessing storm surge hazards.

3.4 Effects of tidal interaction on storm surge response

3.4.1 Spatial distribution of water levels

To further examine the role of tidal interaction, Fig. 11 shows the spatial distributions of maximum water levels generated by synthetic typhoon No. 28 (P_c = 952.99 hPa, V_{max} = 46.31 m/s, R_{max} = 35.19 km, and D_{min} = 148.11 km) under SSO and TSSI conditions. Figure 11(a) shows the MSSH obtained from the SSO simulation,(14) which excludes tidal effects, whereas Fig. 11(b) presents the MWSH that results from the nonlinear superposition of tides and storm surge under TSSI conditions.

In the SSO simulation [Fig. 11(a)], storm surge heights of approximately 1.0–1.5 m appear along the Yeonggwang–Boryeong coastline, including the HNPP site. The surge forms a narrow band concentrated along the coastline aligned with the typhoon's forward path. Because the typhoon remains relatively distant from the coast, the spatial extent of surge influence is limited. In contrast, the TSSI simulation [Fig. 11(b)] shows a substantially amplified and expanded water-level response as tidal variations are superimposed on the surge. Wide coastal regions exceed 3 m in total water level, and water levels of 3.0–3.5 m or higher are evident between Boryeong and Yeonggwang. Compared with the SSO condition, the TSSI results reveal not only a significant increase in absolute water levels but also a pronounced expansion of the spatial impact area. This behavior is closely associated with the complex coastline and the macrotidal characteristics of the western coast of Korea.

3.4.2 Time-series comparison at the HNPP site

Figure 12 shows the time-series water-level variations at the HNPP site obtained from both SSO and TSSI simulations. Under SSO conditions, the MSSH reaches 1.23 m, and the storm surge hydrograph exhibits a relatively broad temporal spread. Under TSSI conditions, however, nonlinear interactions between tide and surge increase the MWSH to 3.48 m. The rising and falling limbs of the hydrograph also become steeper than those of the tide alone. This amplification occurs because the peak storm surge coincides with the tidal high-water phase, resulting in constructive superposition and a substantial elevation of the peak water level.

3.4.3 Extracted storm surge components under TSSI conditions

To quantitatively isolate the inherent storm surge characteristics under TSSI conditions, the tidal components associated with the eight major constituents (M_2, S_2, N_2, K_2, K_1, O_1, P_1, Q_1)

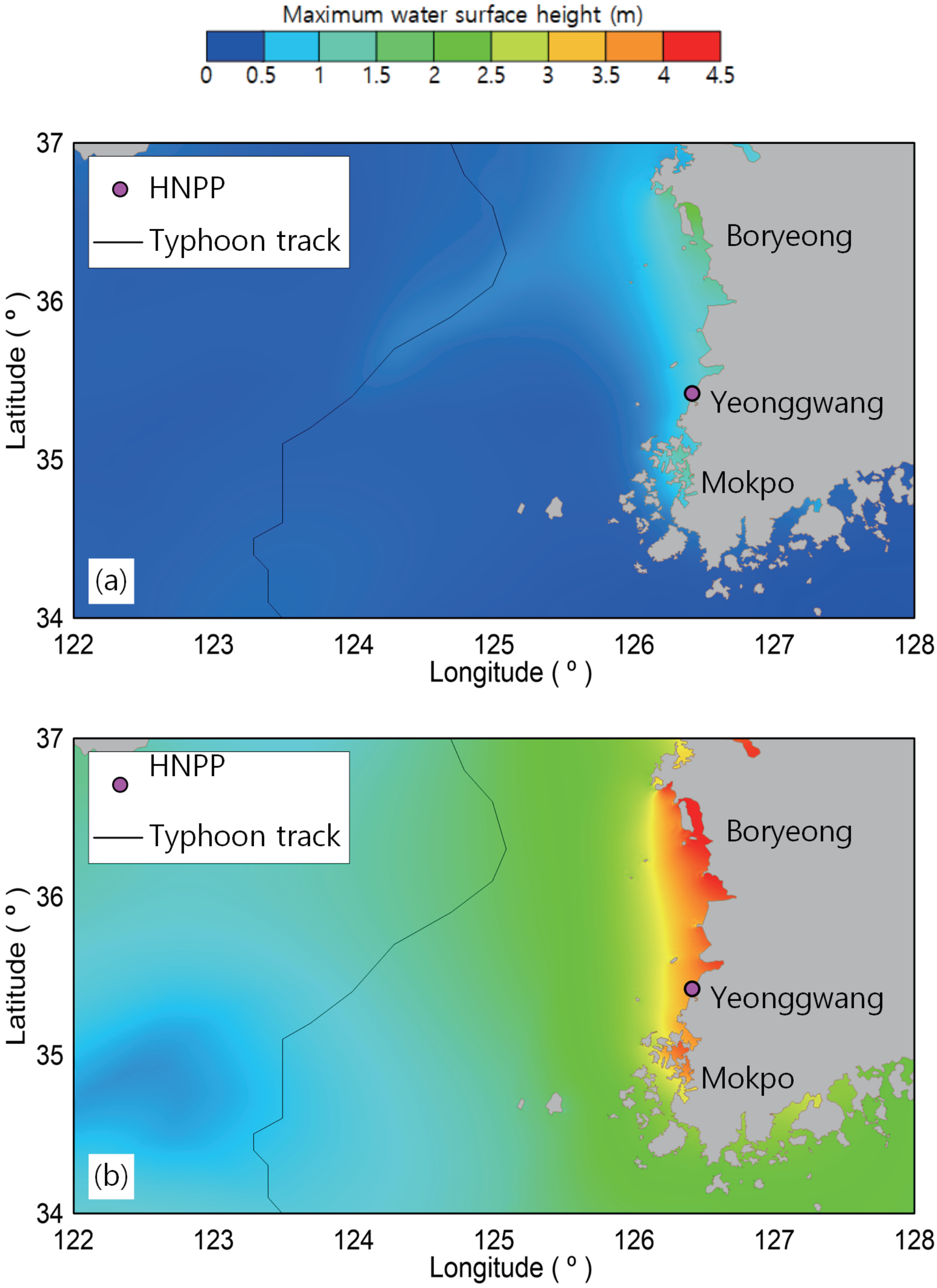

Fig. 11. (Color online) Spatial distribution of (a) SSO-based MSSH and (b) TSSI-based MWSH generated by synthetic typhoon No. 28.

were removed by the harmonic decomposition of the simulated water-level time series. The resulting residual storm surge hydrographs were used to compute MSSH and time-integrated storm surge height (TISSH). Their relationships with typhoon parameters (P_c, $V_{\max}$, $R_{\max}$, and $D_{\min}$), together with comparisons with SSO results, are shown in Figs. 13 and 14.

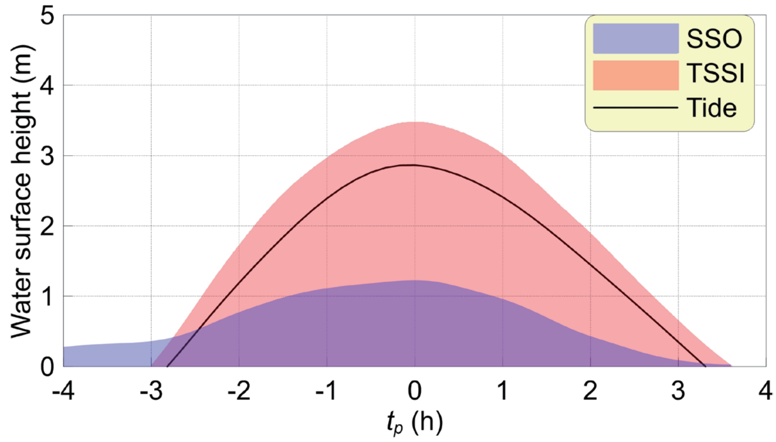

Fig. 12. (Color online) Time series of SSO-based and TSSI-based water-surface heights at the HNPP site.

The MSSH and TISSH values derived from the TSSI simulations are consistently lower than those from the SSO analysis. On average, the TSSI-based MSSH and TISSH correspond to 70.94 and 77.19% of the SSO values, respectively. This reduction indicates that nonlinear TSSI suppresses the development and amplification of the storm surge component. In a macrotidal environment, tidal forcing modifies the sea-surface slope, velocity field, and bottom-friction conditions. These changes cause the hydrodynamic response of the storm surge component superimposed on the astronomical tide to differ from that obtained under SSO conditions, thereby attenuating the extracted storm surge component.

The effect of typhoon parameters on MSSH differs substantially between the SSO and TSSI simulations. As shown in Fig. 13, the fundamental trend remains the same, with lower P_c, higher $V_{\max}$, smaller $R_{\max}$, and shorter $D_{\min}$ leading to larger MSSH. However, the regression slopes from the TSSI analysis are smaller than those from the SSO analysis, indicating that the direct effect of typhoon intensity weakens in the presence of tides. The difference between the two analyses becomes more pronounced for stronger typhoons with low P_c, high $V_{\max}$, and small $R_{\max}$ as well as for those that pass closer to HNPP. This indicates that nonlinear attenuation becomes stronger when storm forcing increases. A similar pattern is observed for TISSH in Fig. 14, although the effect of $D_{\min}$ is comparatively limited. This limited sensitivity reflects the same island-sheltered coastal geometry near HNPP, which reduces the dependence of surge volume on typhoon proximity.

A comparison of the SSO-based MSSH added linearly to the peak tidal level of 2.86 m and the TSSI-derived MWSH shows that the latter corresponds to 94.76% of the linear sum. In other words, the TSSI-derived peak water level is 5.24% lower than the level obtained through linear

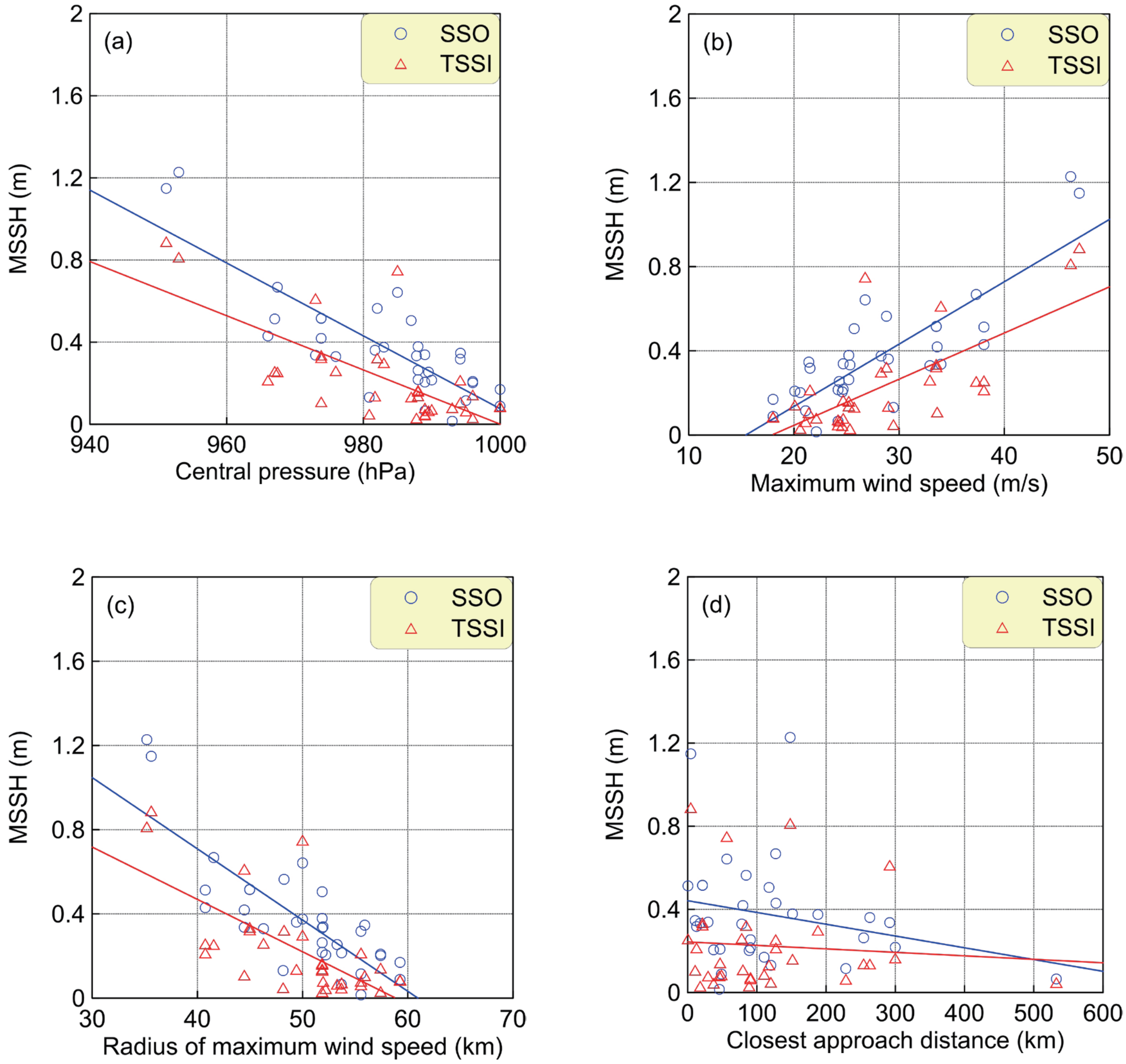

Fig. 13. (Color online) Scatter plots of SSO-based and TSSI-based MSSH at the HNPP site as functions of (a) P_c, (b) V_{max}, (c) R_{max}, and (d) D_{min}.

superposition. This difference indicates that the peak total water level under TSSI conditions is governed by nonlinear tide–surge interaction rather than by simple linear addition. In the macrotidal West Sea, the astronomical tide modifies the hydrodynamic conditions under which the storm surge component develops, including tidal phase, sea-surface slope, velocity field, and bottom-friction response. Therefore, the TSSI-derived MWSH can be lower than the linearly superimposed value even when the total water level is substantially elevated by the tide. Overall, the results indicate that TSSI-based analysis is essential for accurately assessing typhoon-induced coastal hazards in this macrotidal setting.

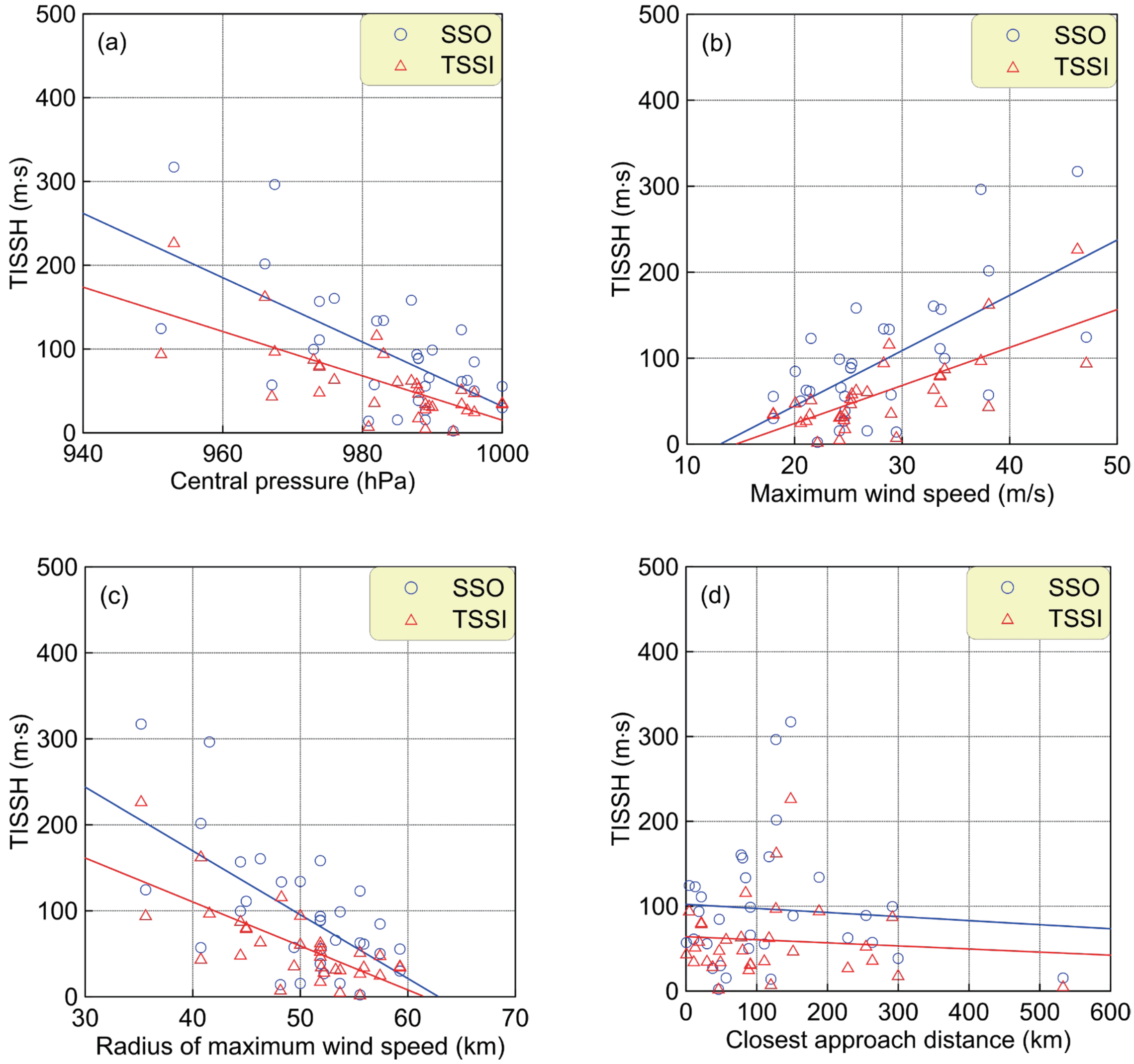

Fig. 14. (Color online) Scatter plots of SSO-based and TSSI-based TISSH at the HNPP site as functions of (a) P_c, (b) V_{max}, (c) R_{max}, and (d) D_{min}.

3.5 Sensitivity analysis

3.5.1 Analytical methods

To quantify the sensitivity of storm surge responses (MSSH and TISSH) to typhoon parameters, Pearson correlation coefficients (γ) and standardized ridge regression coefficients (β_{ridge}) were jointly applied. γ was used to examine the linear bivariate relationships between each explanatory variable and the response variables, whereas β_{ridge} was used to assess the conditional contribution of each parameter while accounting for inter-variable dependence. The latter approach allows stable estimation even when substantial collinearity exists among typhoon parameters.

The linear bivariate relationship between each explanatory variable X_j (P_c, $V_{\max}$, $R_{\max}$, and, $D_{\min}$) and the response variable Y (MSSH or TISSH) was evaluated using γ, given by

$$\gamma = \frac{\sum_{i=1}^{n}\left(X_{ij} - \overline{X_j}\right)\left(Y_i - \overline{Y}\right)}{\sqrt{\sum_{i=1}^{n}\left(X_{ij} - \overline{X_j}\right)^2}\sqrt{\sum_{i=1}^{n}\left(Y_i - \overline{Y}\right)^2}}. \quad (14)$$

This metric indicates the overall linear tendency and direction between each typhoon parameter and the storm surge response. However, because meteorological characteristics and track-related factors are often strongly interrelated, the individual effects of each parameter cannot be clearly distinguished using simple correlations alone. To address this limitation, all explanatory variables and response variables were standardized to zero mean and unit variance, and the following standardized regression model was applied:

$$Z_Y = \beta_0 + \sum_{j=1}^{4} \beta_j Z_{X_j} + \varepsilon, \quad (15)$$

where β_0 is the standardized intercept, β_j is the standardized regression coefficient, and ε denotes the error term. The standardized variables are defined as

$$Z_{X_j} = \frac{X_{ij} - \overline{X_j}}{s_{X_j}}, Z_Y = \frac{Y_i - \overline{Y}}{s_Y}, \quad (16)$$

where s_{X_j} and s_Y are the standard deviations of X_j and Y, respectively. The coefficients (β_j) represent the conditional contributions of each variable after accounting for the effects of the remaining parameters, allowing direct comparison across variables with differing physical units.

Because typhoon parameters often exhibit strong meteorological and track-related interdependence, multicollinearity may arise and result in unstable or misleading regression coefficients. To mitigate this issue, ridge regularization with an L_2 penalty was applied. β_{ridge} is obtained by solving

$$\beta_{ridge} = \arg_{\beta}^{min} \left\{ \left\| Z_Y - Z_X \beta \right\|_2^2 + \lambda \left\| \beta \right\|_2^2 \right\}, \quad (17)$$

where Z_X is the standardized design matrix, Z_Y is the standardized response vector, and λ is the regularization parameter.

In this study, the optimal value of λ for each analysis was determined by minimizing the mean squared error (MSE) through fivefold cross-validation. Ridge regression thereby provides stable estimates of the conditional contributions of the typhoon parameters in the presence of multicollinearity.

3.5.2 Sensitivity of typhoon parameters

The sensitivity analysis results presented in Table 1 quantify how the typhoon parameters affect the storm surge responses under both SSO and TSSI conditions. γ represents the bivariate linear association between each variable and the response variable, whereas β_{ridge} indicates the conditional contribution of each parameter after controlling for the effects of all remaining variables.

According to the data in Table 1, the meteorological parameters (P_c, $V_{\max}$, and $R_{\max}$) exert substantially stronger effects on both MSSH and TISSH than $D_{\min}$. The Pearson correlation results show consistent relationships under both SSO and TSSI conditions, with lower P_c, higher $V_{\max}$, and smaller $R_{\max}$, associated with greater MSSH and TISSH, whereas $D_{\min}$ consistently shows the weakest association. These results indicate that storm surge characteristics at the HNPP site are governed primarily by typhoon intensity and structure, while the typhoon's proximity plays a secondary role.

For MSSH, the ridge regression results indicate that P_c and $R_{\max}$ make greater conditional contributions than $V_{\max}$ and $D_{\min}$. Although the relative importance of P_c and $R_{\max}$ differs between SSO and TSSI, both parameters consistently exhibit substantial contributions, whereas $V_{\max}$ shows a secondary contribution. This indicates that MSSH is strongly affected by both typhoon intensity and the spatial structure of the wind field when inter-variable dependence is considered. The lowest sensitivity of $D_{\min}$ arises from the island-shielded shallow-water environment near HNPP, which modulates storm surge propagation and reduces proximity-related effects.

For TISSH, $V_{\max}$ exhibits the greatest conditional contribution, followed by P_c and $R_{\max}$, under both SSO and TSSI conditions. This consistent ordering indicates that $V_{\max}$ plays a particularly important role in the integrated storm surge response. The effect of $D_{\min}$ remains the smallest, demonstrating again that storm surge responses at HNPP are dominated by typhoon intensity and structure rather than proximity.

Comparison of the SSO and TSSI results shows that tidal interaction does not uniformly reduce the sensitivity of storm surge responses to the typhoon parameters. Instead, TSSI modifies their relative contributions, particularly for MSSH, indicating that nonlinear tide–surge interaction alters the response to individual typhoon parameters.

Table 1
Pearson correlation coefficients and standardized ridge regression coefficients for each typhoon parameter.

Analysis	Result	Coefficient	P_c	$V_{\max}$	$R_{\max}$	$D_{\min}$
SSO	MSSH	γ	−0.822	0.823	−0.804	−0.242
		β_{ridge}	−1.137	0.469	0.802	−0.191
	TISSH	γ	−0.648	0.651	−0.643	−0.075
		β_{ridge}	−0.197	0.206	−0.184	−0.028
TSSI	MSSH	γ	−0.572	0.573	−0.551	−0.187
		β_{ridge}	−1.016	0.572	1.034	−0.150
	TISSH	γ	−0.528	0.531	−0.513	−0.135
		β_{ridge}	−0.172	0.182	−0.123	−0.082

Overall, typhoon intensity and structure are the principal drivers of storm surge hazards at the HNPP site, while $D_{\min}$ plays a comparatively minor role. Considering the sensitivity results collectively, with the ridge regression results used to assess conditional contributions under inter-variable dependence, the sensitivity hierarchy is summarized as follows.

- MSSH: $P_c > R_{\max} > V_{\max} > D_{\min}$
- TISSH: $V_{\max} > P_c > R_{\max} > D_{\min}$

4. Conclusions

In this study, we quantitatively examined the nonlinear interactions between tides and storm surge at the HNPP, located along Korea's macrotidal west coast. Using 33 synthetic typhoons generated by the TCRM, we conducted TSSI simulations with the ADCIRC model. Model performance was validated against continuous water-level records from tide-gauge sensor networks at 19 coastal stations during Typhoons Muifa (1109) and Bolaven (1215), confirming the reliability of both tidal-phase representation and maximum water-level reproduction. These results demonstrate that the spatial coverage and measurement fidelity of water-level sensing networks are essential for validating coupled hydrodynamic simulations and for ensuring the reliability of storm surge hazard assessments at coastal nuclear facilities.

The numerical results show that nonlinear TSSI substantially increases both the spatial extent and absolute magnitude of total water levels. However, the intrinsic storm surge components extracted through harmonic decomposition (MSSH and TISSH) are reduced to 70.94 and 77.19% of the SSO results, respectively. This reduction reflects nonlinear attenuation associated with changes in tidal phase, tidal current strength, sea-surface slope, and bottom-friction response, which suppress the development of the surge component. Furthermore, the average TSSI-based MWSH corresponds to 94.76% of the linear sum of SSO-based MSSH and the peak tidal level (2.86 m), indicating that linear superposition may overestimate the peak total water level in this macrotidal setting.

The sensitivity analysis identified distinct parameter hierarchies for the two storm surge responses: $P_c > R_{\max} > V_{\max} > D_{\min}$ for MSSH and $V_{\max} > P_c > R_{\max} > D_{\min}$ for TISSH. In both cases, $D_{\min}$ was the least influential, while tidal interaction altered the relative contributions of the typhoon parameters rather than uniformly reducing their sensitivities. These findings demonstrate that the tidal phase at landfall is as important as typhoon intensity in determining extreme water-level hazards in this macrotidal environment.

The results of this study emphasize the necessity of incorporating TSSI into hazard assessments for coastal nuclear power plant sites along the West Sea coast and highlight the limitations of linear-superposition-based approaches. As this study was focused on a single site along the West Sea coast, future research should extend the analysis to the East Sea, where most Korean nuclear power plants are located and where tidal ranges are smaller and water depths are greater. Comparisons between TSSI and existing SSO analyses[27] will provide further insight into the distinct interaction mechanisms governing storm surge in deep and microtidal environments. Because the present simulations did not include wave-model coupling, wave-induced setup and runup were not resolved. Accordingly, the estimated MWSH should be interpreted as the tide- and surge-induced water level and may be locally underestimated where wave effects are significant. Future research will also involve assessing storm wave hazards,[28] evaluating future extreme water levels under SLR scenarios, and developing an integrated multihazard risk assessment framework that encompasses tsunami-induced inundation[29] and drifting–collision[30,31] hazards posed by large waterborne debris.

Acknowledgments

This work was supported by a National Research Foundation of Korea (NRF) grant funded by the Korean government (MSIT) (RS-2022-00144263).

References

1 L. Li, Z. Li, Z. He, Z. Yu, and Y. Ren: Front. Mar. Sci. **9** (2022) 890285. https://doi.org/10.3389/fmars.2022.890285
2 J. L. Rego and C. Li: J. Geophys. Res. Oceans **115** (2010) C06020. https://doi.org/10.1029/2009JC005285
3 D. Idier, F. Dumas, and H. Muller: Nat. Hazards Earth Syst. Sci. **12** (2012) 3709. https://doi.org/10.5194/nhess-12-3709-2012
4 W. Zhang, L. Teng, J. Zhang, M. Xiong, and C. Yin: J. Oceanol. Limnol. **37** (2019) 2037. https://doi.org/10.1007/s00343-019-8277-8
5 Z. Xiao, Z. Yang, T. Wang, N. Sun, M. Wigmosta, and D. Judi: Front. Mar. Sci. **8** (2021) 715557. https://doi.org/10.3389/fmars.2021.715557
6 S. Barbot, L. Pineau-Guillou, and J. M. Delouis: J. Geophys. Res. Oceans **129** (2024) e2023JC020772. https://doi.org/10.1029/2023JC020772
7 J. C. M. Dullaart, S. Muis, H. de Moel, P. J. Ward, D. Eilander, and J. C. J. H. Aerts: Nat. Hazards Earth Syst. Sci. **23** (2023) 1847. https://doi.org/10.5194/nhess-23-1847-2023
8 C. Antony, A. S. Unnikrishnan, Y. Krien, P. L. N. Murty, S. V. Samiksha, and A. K. M. S. Islam: Reg. Stud. Mar. Sci. **35** (2020) 101133. https://doi.org/10.1016/j.rsma.2020.101133
9 S. Muis, M. I. Apecechea, J. Dullaart, J. de Lima Rego, K. S. Madsen, J. Su, K. Yan, and M. Verlaan: Front. Mar. Sci. **7** (2020) 263. https://doi.org/10.3389/fmars.2020.00263
10 M. De Dominicis, J. Wolf, S. Jevrejeva, P. Zheng, and Z. Hu: Geophys. Res. Lett. **47** (2020) e2020GL087002. https://doi.org/10.1029/2020GL087002
11 X. Zhang, D. Chu, and J. Zhang: Nat. Hazards **107** (2021) 551. https://doi.org/10.1007/s11069-021-04595-y
12 Y. Chen, Y. Miao, P. Xie, Y. Zhang, and Y. Li: Front. Mar. Sci. **11** (2024) 1423294. https://doi.org/10.3389/fmars.2024.1423294
13 H. J. Kim, H. Jin, B. I. Min, and W. D. Lee: J. Ocean Eng. Technol. **39** (2025) 152. https://doi.org/10.26748/KSOE.2025.011
14 H. J. Kim, T. Hwang, B. I. Min, M. Seo, and W. D. Lee: J. Ocean Eng. Technol. **39** (2025) 512. https://doi.org/10.26748/KSOE.2025.035
15 R. A. Luettich, J. J. Westerink, and N. W. Scheffner: Tech. Rep. DRP-92-6 (U.S. Army Engineer Waterways Experiment Station, Vicksburg, MS, 1992).
16 R. O. Reid: Handbook of Coastal and Ocean Engineering, J. B. Herbich, Ed. (Gulf Publishing Co., Houston, TX, 1990).
17 P. Schureman: Spec. Publ. No. 98 (U.S. Coast and Geodetic Survey, U.S. Dept. of Commerce, Government Printing Office, Washington, DC, 1941).
18 M. G. G. Foreman: Pac. Mar. Sci. Rep. 77-10 (Inst. of Ocean Sciences, Patricia Bay, Sidney, BC, 1977).
19 G. J. Holland: Mon. Weather Rev. **108** (1980) 1212. https://doi.org/10.1175/1520-0493(1980)108<1212:AAMOTW>2.0.CO;2
20 H. J. Kim and S. W. Suh: J. Coast. Res. **75** (2016) 1132. https://doi.org/10.2112/SI75-227.1
21 N. W. Summons and W. C. Arthur: Tropical Cyclone Risk Model User Guide (Commonwealth of Australia, Canberra, 2011).
22 J. Gahtan, K. R. Knapp, C. J. Schreck, H. J. Diamond, J. P. Kossin, and M. C. Kruk: NOAA National Centers for Environmental Information, International Best Track Archive for Climate Stewardship (IBTrACS) Version 4r01 (2024). https://doi.org/10.25921/82ty-9e16

23 H. Jin, T. Hwang, H. J. Kim, B. I. Min, and W. D. Lee: J. Korea Water Resour. Assoc. **57** (2024) 1037. https://doi.org/10.3741/JKWRA.2024.57.12.1037
24 W. D. Lee, G. S. Yeom, J. Kim, S. Lee, and T. Kim: Ocean Eng. **259** (2022) 111897. https://doi.org/10.1016/j.oceaneng.2022.111897
25 W. D. Lee, N. Mizutani, and T. Kim: Estuar. Coast. Shelf Sci. **291** (2023) 108434. https://doi.org/10.1016/j.ecss.2023.108434
26 S. A. Hsu and Z. Yan: J. Coast. Res. **14** (1998) 667.
27 T. Hwang, H. J. Kim, B. I. Min, M. Seo, and W. D. Lee: J. Ocean Eng. Technol. **39** (2025) 611. https://doi.org/10.26748/KSOE.2025.039
28 S. C. Seo, H. J. Kim, T. Hwang, and W. D. Lee: J. Coast. Res. **39** (2023) 129. https://doi.org/10.2112/JCOASTRES-D-22TM-00001.1
29 T. Kim, T. Hwang, S. Baek, S. Hong, J. Kim, and W. D. Lee: J. Earthq. Tsunami **17** (2023) 2350016. https://doi.org/10.1142/S1793431123500161
30 W. D. Lee, T. Kim, J. Kim, S. K. Kim, H. Oh, and T. Hwang: J. Ocean Eng. Technol. **38** (2024) 282. https://doi.org/10.26748/KSOE.2024.070
31 T. Hwang, T. Kim, J. Kim, Y. Kim, and W. D. Lee: J. Earthq. Tsunami **18** (2024) 2450010. https://doi.org/10.1142/S1793431124500106

About the Authors

Taegeon Hwang completed his Ph.D. coursework in the Department of Ocean Civil Engineering at Gyeongsang National University, Republic of Korea, in 2024. Since 2025, he has been working as a researcher at the Institute of Marine Industry, Gyeongsang National University. His research interests include the drifting behavior of waterborne debris generated by storm surges and tsunamis, impact force prediction, coastal vulnerability assessment, and coastal secondary disaster analysis. (stg5372@gnu.ac.kr)

Hyeon-Jeong Kim received his Ph.D. degree in ocean construction engineering from Kunsan National University, Republic of Korea, in 2019. From 2020 to 2021, he was a senior researcher at the National Disaster Management Institute. From 2021 to 2022, he served as a senior researcher in the R&D Department of The Haebon Co., Ltd. He is currently a senior researcher at the Korea Atomic Energy Research Institute. His research interests include coastal hydrodynamics, storm surge risk assessment, and climate change impact analysis on coastal hazards. (liswjd@kaeri.re.kr)

Byung-Il Min received his Ph.D. degree in coastal and ocean engineering from Sungkyunkwan University, Republic of Korea, in 2011. From 2008 to 2010, he worked as a senior researcher at the Marine Information Technology Institute, and from 2011 to 2012, he served as a research fellow at the Construction and Environmental Systems Engineering Research Institute of Sungkyunkwan University. Since 2012, he has been a principal researcher at the Korea Atomic Energy Research Institute. His research interests include natural hazards such as earthquakes, tsunamis, floods, and storm surges. (bimin@kaeri.re.kr)

Minjang Seo received his M.S. degree in ocean civil engineering from Gyeongsang National University, Republic of Korea, in 2023. Since 2023, he has been working as an engineer in the Harbor & Coastal Department at Yooshin Engineering Corporation. His research interests include landslide-generated tsunamis, fluid–structure interaction analysis, storm surge simulation, hydraulic model experiments, and port and coastal structure design. (smj7467@yooshin.com)

Woo-Dong Lee received his Ph.D. degree in coastal and ocean engineering from Nagoya University, Japan, in 2012. From 2012 to 2017, he worked as a research fellow at the Institute of Marine Industry, Gyeongsang National University, Republic of Korea. Since 2017, he has been a professor in the Department of Ocean Civil Engineering at Gyeongsang National University. His research interests include numerical modeling, hydraulic experiments, coastal hazard assessment, marine disasters, and diving engineering. (wdlee@gnu.ac.kr)